Active control of road vehicle's drag for varying upstream flow conditions using a recursive subspace based predictive control methodology

Agostino Cembalo, Patrick Coirault, Jacques Borée, Clément Dumand, Guillaume Mercère

Active control of road vehicle's drag for varying upstream flow conditions using a Recursive Subspace based Predictive Control methodology

Agostino Cembalo[a,c], Patrick Coirault[b,*], Jacques Borée[a], Clément Dumand[c], Guillaume Mercère[b]

[a] *Pprime Institute CNRS, ENSMA, University of Poitiers, 1 Av. Clément Ader, 86360 Chasseneuil-du-Poitou, France*
[b] *Laboratory LIAS - ENSIP, University of Poitiers, 2 rue Pierre Brousse, 86073 Poitiers, France*
[c] *STELLANTIS, Advanced Innovation, 212 Bd Pelletier, 78955 Carrières-sous-Poissy,France*

Abstract

The growing focus on reducing energy consumption, particularly in electric vehicles with limited autonomy, has prompted innovative solutions. In this context, we propose a real-time flap-based control system aimed at improving aerodynamic drag in real driving conditions. Employing a Recursive Subspace based Predictive Control approach, we conducted wind tunnel tests on a representative model vehicle at reduced scale equipped with flaps. Comprehensive assessments using pressure measurements and Particle Image Velocimetry were undertaken to evaluate the control efficiency. Static and dynamic perturbation tests were conducted, revealing the system's effectiveness in both scenarios. The closed-loop controlled system demonstrated a substantial gain, achieving a 5% base pressure recovery.

Keywords: aerodynamics, adaptive flow control, drag reduction, recursive subspace based predictive control, experiments, road vehicles

1. Introduction

Worldwide, vehicle manufacturers put increasing emphasis on the reduction of their vehicles environmental footprint as well as the reduction of energy consumption. Their goal is to produce affordable, reliable, and environmentally friendly vehicles while simultaneously reducing the total cost of ownership for their customers. The aerodynamic performance of vehicles plays a crucial role in achieving these objectives, as there is a strong correlation between aerodynamic drag and energy consumption. At highway speeds, approximately 70% of the energy losses can be attributed to aerodynamic forces (Kadijk and Ligterink 23, Hucho and Sovran 19) and these losses are known to increase as the cube of the velocity.

For a given vehicle project, reducing the aerodynamic drag is therefore a key objective of car manufacturers. This optimization process is conducted by combining computational fluid dynamics and expensive wind tunnel tests at real scale. All these steps however only correspond to approximations of the real driving performance of the vehicles because they are conducted in steady state situations. In real-life scenarios, because of the variety of operating conditions that any vehicle has to face over its life-cycle, the vehicle is subject to a continuous inputs from the natural wind and the wake of other vehicles. A lot of studies have been devoted to characterizing the effects of changes in the surrounding environments (Cooper and Watkins 11, Watkins and Cooper 38, Schröck et al. 32, Garcia de la Cruz et al. 12). Using quasi-steady solution, a wind averaged drag coefficient can be defined using representative wind-speed distributions (Howell et al. 17). This wind averaged drag coefficient is significantly higher than the basic drag coefficient at zero yaw. As stressed by these authors, reducing the sensitivity of the aerodynamic loads to the natural wind is therefore a critical issue for aerodynamic development engineers. Starting from these considerations, the objective of this research is therefore, for varying upstream flow conditions, to use active flow control in order to maintain the drag performance at zero yaw angle. More specifically, in this work the primary focus is on the control of the wake, as it has a predominant role in contributing to the overall pressure drag.

Numerous studies, not detailed here for brevity, demonstrate that the major contributor to the increase of the pressure drag for varying upstream flow conditions is the large scale near wake region developing at the back of the vehicle. For perturbed upstream conditions, this near wake looses its average symmetry, which results in an increase of base drag (see Haffner et al. 16 for a recent review). For small deviations from the reference situation, passive or active actuation can be designed to compensate these asymmetries of the near wake, either by imposing local flow deviations using tapers or flaps – a strategy called "pressure control" – or by modifying the turbulent properties of the unsteady shear layers surrounding the near wake – a strategy called "turbulence control". For example, for small yaw angles representative of real driving conditions, for steady situations, mechanical flaps (Urquhart et al. 35, Urquhart and Sebben 34)), tapers (Varney et al. 36, Perry et al. 31)) or even high frequency pulsed jets (Li et al. 25) have been shown to be effective in cancelling yaw induced asymmetries of the large recirculating

Patrick Coirault, Bâtiment B25, 2 rue Pierre Brousse, TSA 41105, 86073 Poitiers cedex 9.
Email address: patrick.coirault@univ-poitiers.fr (P. Coirault)

region, leading to a significant decrease of drag. It therefore seems a natural idea to configure an adaptative system with the ability to adapt to any given real-world yaw condition. This is the objective of the present research making use of actuated flaps along the edges of the base of the vehicle.

This study is performed using an academic, but representative, model at reduced scale called "Windsor model" (see Pavia et al. 30 and references therein) used in numerous experimental and CFD studies. An accompanying on-road test campaign was also carried by the authors in windy conditions capturing time-dependent data for resultant air-speed, yaw angle, and base pressure distribution using car-mounted instrumentation. Usual probability density functions (pdf) of yaw angles (β) were obtained with typically $-5^\circ \leq \beta \leq 5^\circ$ for 95% of the time (Cembalo 8), which confirms the results of previous research works (Carlino et al. 6, Garcia de la Cruz et al. 12, Stoll and Wiedemann 33, Yamashita et al. 39). The important message from these campaigns is that large scale vertical or horizontal motions of the near wake are indeed detected and are main contributors to the variance of the base pressure fluctuation. Interestingly, low frequency global wake motions have a major contribution in real situations, which makes it interesting to search for quasi-steady active control solution because the time scale of the external forcing of the wake by the slow external perturbations is then much larger than the advective time scale driving unsteady aerodynamic responses. To provide a quantitative analysis, we introduce the dimensionless frequency known as the Strouhal number (St), defined as $St = Hf/V$. This dimensionless number compares the wake motion frequency to the advective time scale H/V, where H and V represent the height of the base and velocity of the vehicle, respectively. For the road tests conducted on a Stellantis vehicle, 49 unsteady pressure sensors were installed on the base, allowing simultaneous data acquisition. Focusing on the asymmetry of the wake, a Proper Orthogonal Decomposition (Berkooz et al. 4) of the on-road pressure data reveals that the two dominant modes correspond to respectively vertical and horizontal large scale wake asymmetry, collectively contributing to over 60% of the total variance. Further spectral analysis of the random coefficients associated with these two modes indicates that low frequencies (typically $St \leq 10^{-1}$) contribute more than 60% of the variance induced by these large-scale asymmetries (Cembalo et al. 9, Cembalo 8). Given these findings, our approach in this study is to explore a quasi-steady control methodology.

In light of these objectives, we propose an investigation into an active solution that revolves around controlling four rigid flaps positioned at the base of the academic model. By employing the flaps, we can manipulate the wake orientation to control the pressure distribution at the base of the model. Additionally, by reducing the actuation frequency —since the goal is to compensate for quasi-static perturbations due to environmental changes— we can significantly decrease the energy required to control the system.

Wind tunnel investigations have demonstrated that the aerodynamic drag of a vehicle is significantly influenced by the fluctuating upstream flow conditions. Nevertheless, due to practical constraints in industrial settings, accurately measuring these upstream flow conditions is not feasible on each vehicle while driving on the road. From a control perspective, this implies that the upstream flow conditions are treated as an unknown disturbance influencing the dynamics of the system. Due to the inherent complexity of the Navier-Stokes equations, establishing a input/output dynamic model for the system grounded in physical laws becomes unfeasible. Henceforth, our proposal involves the online identification of a black-box discrete-time Linear Time-Varying model derived from experimental data. In addressing both the constraints imposed by flap angle saturation and the absence of state measurements, we developed a Recursive Subspace-based Predictive Control approach. In the closed-loop system, input/output data are intricately correlated with noise, and we propose an unbiased recursive estimator to mitigate these challenges. This approach ensures that the proposed solution remains economically viable, aligning with the industrial feasibility criteria. The latter offers the advantage of recursive estimation, allowing the control system to continuously update and refine its model based on real-time measurements. This adaptive capability enhances the robustness and accuracy of the control process, ensuring consistent performance over time and maximizing the drag reduction over the wide range of operating conditions.

The paper is organized as follows: Section 2 provides an introduction of the notations and definitions employed in this study. In Section 3, we delve into the system description, covering experimental setup, equipment, instrumentation and the test environment. Section 4 introduces the control law, delineating design principles and algorithms. Moving on to Section 5, we present experimental results and conduct a performance analysis of the control law. Within this section, we discuss the selection of control objectives and evaluate the implemented control law's performance. The work concludes with a concise summary in which key findings are highlighted for their significance in achieving the research objectives. Additionally, potential avenues for future investigation are proposed.

2. Notations and definitions

This section presents the notations and useful definitions used in the paper.

Let $\mathbb{N}$ and $\mathbb{R}$ be the sets of positive integers and real numbers, respectively. $\mathbb{N}^*$ denotes the set of positive non-zero integers. The set of real column vectors of dimension $n \in \mathbb{N}^*$ is denoted by $\mathbb{R}^n$ and the set of real matrices of $n \in \mathbb{N}^*$ rows and $m \in \mathbb{N}^*$ columns is denoted by $\mathbb{R}^{n\times m}$. For a vector $\boldsymbol{x}(k) \in \mathbb{R}^{n_x}$, $\Delta\boldsymbol{x}(k) = \boldsymbol{x}(k) - \boldsymbol{x}(k-1)$. $(\boldsymbol{x}(i))_{i=k}^{k+\ell-1}$ denotes the time sequence $\boldsymbol{x}(k),\ \ldots,\ \boldsymbol{x}(k+\ell-1)$. Given a rectangular matrix $\boldsymbol{M} \in \mathbb{R}^{n\times m}$, its transpose is denoted by $\boldsymbol{M}^\top \in \mathbb{R}^{m\times n}$, $\boldsymbol{M}^{(i)} \in \mathbb{R}^{1\times m}$ represents its i^{th} row. The Moore-Penrose pseudo inverse of a rectangular matrix $\boldsymbol{M}$ is denoted by $\boldsymbol{M}^\dagger$. For any vector $\boldsymbol{x}(k) \in \mathbb{R}^{n_x}$, with $k \in \mathbb{N}$, the finite vector over a specific window of size ℓ steps

($\ell \in \mathbb{N}^*$) starting from a specified instant $k \in \mathbb{N}$ is denoted as

$$\boldsymbol{X}_{k,\ell,1} = \begin{bmatrix} \boldsymbol{x}(k) \\ \boldsymbol{x}(k+1) \\ \vdots \\ \boldsymbol{x}(k+\ell-1) \end{bmatrix} \in \mathbb{R}^{n_x \ell}. \tag{1}$$

Accordingly, the block Hankel matrix containing the available data starting from instant $k \in \mathbb{N}$ distributed over $\ell \in \mathbb{N}^*$ rows and $M \in \mathbb{N}^*$ columns is denoted as

$$\boldsymbol{X}_{k,\ell,M} = \begin{bmatrix} \boldsymbol{X}_{k,\ell,1} & \boldsymbol{X}_{k+1,\ell,1} & \cdots & \boldsymbol{X}_{k+M-1,\ell,1} \end{bmatrix} \in \mathbb{R}^{n_x \ell \times M}. \tag{2}$$

The norm of the vector $\|\boldsymbol{X}_{k,\ell,1}\|_{\boldsymbol{Q}}^2$ denotes the quadratic form $\boldsymbol{X}_{k,\ell,1}^\top \boldsymbol{Q} \boldsymbol{X}_{k,\ell,1}$ where $\boldsymbol{Q} \in \mathbb{R}^{n_x \ell \times n_x \ell}$ is a symmetric definite positive matrix. The following matrices are defined by

$$\boldsymbol{S}_{\ell,n} = \begin{bmatrix} \mathbb{I}_{n\times n} & \mathbb{O}_{n\times n} & \cdots & \cdots \\ \mathbb{I}_{n\times n} & \mathbb{I}_{n\times n} & \mathbb{O}_{n\times n} & \cdots \\ \vdots & \vdots & \ddots & \vdots \\ \mathbb{I}_{n\times n} & \mathbb{I}_{n\times n} & \mathbb{I}_{n\times n} & \mathbb{I}_{n\times n} \end{bmatrix} \in \mathbb{R}^{\ell n \times \ell n}, \tag{3}$$

$$\mathbb{1}_{\boldsymbol{\ell},\boldsymbol{n}} = \begin{bmatrix} \mathbb{I}_{n\times n} \\ \vdots \\ \mathbb{I}_{n\times n} \end{bmatrix} \in \mathbb{R}^{\ell n \times n}. \tag{4}$$

Let us consider the state representation of a discrete time LTI system

$$\begin{aligned} \boldsymbol{x}(k+1) &= \boldsymbol{A}\boldsymbol{x}(k) + \boldsymbol{B}\boldsymbol{u}(k) \\ \boldsymbol{y}(k) &= \boldsymbol{C}\boldsymbol{x}(k) + \boldsymbol{D}\boldsymbol{u}(k) \end{aligned}$$

where $\boldsymbol{x} \in \mathbb{R}^{n_x}$ is the state vector, $\boldsymbol{u} \in \mathbb{R}^{n_u}$ is the input and $\boldsymbol{y} \in \mathbb{R}^{n_y}$ is the output. Using the state-space matrices $\boldsymbol{A} \in \mathbb{R}^{n_x \times n_x}$, $\boldsymbol{B} \in \mathbb{R}^{n_x \times n_u}$, $\boldsymbol{C} \in \mathbb{R}^{n_y \times n_x}$ and $\boldsymbol{D} \in \mathbb{R}^{n_y \times n_u}$ and an integer $\ell > 0$, the controlability matrix is defined as

$$\mathcal{K}_\ell(\boldsymbol{A}, \boldsymbol{B}) = \begin{bmatrix} \boldsymbol{A}^{\ell-1}\boldsymbol{B} & \cdots & \boldsymbol{A}\boldsymbol{B} & \boldsymbol{B} \end{bmatrix} \in \mathbb{R}^{n_x \times \ell n_u}, \tag{5}$$

the observability matrix is given by

$$\boldsymbol{\Gamma}_\ell(\boldsymbol{A}, \boldsymbol{C}) = \begin{bmatrix} \boldsymbol{C} \\ \boldsymbol{C}\boldsymbol{A} \\ \boldsymbol{C}\boldsymbol{A}^2 \\ \vdots \\ \boldsymbol{C}\boldsymbol{A}^{\ell-1} \end{bmatrix} \in \mathbb{R}^{\ell n_y \times n_x}, \tag{6}$$

and the block-Toeplitz matrix $\boldsymbol{H}_\ell(\boldsymbol{A}, \boldsymbol{B}, \boldsymbol{C}, \boldsymbol{D}) \in \mathbb{R}^{\ell n_y \times \ell n_u}$ is defined as follows

$$\boldsymbol{H}_\ell(\boldsymbol{A}, \boldsymbol{B}, \boldsymbol{C}, \boldsymbol{D}) = \begin{bmatrix} \boldsymbol{D} & 0 & \dots & 0 \\ \boldsymbol{C}\boldsymbol{B} & \boldsymbol{D} & \dots & 0 \\ \vdots & \ddots & \ddots & \vdots \\ \boldsymbol{C}\boldsymbol{A}^{\ell-2}\boldsymbol{B} & \dots & \boldsymbol{C}\boldsymbol{B} & \boldsymbol{D} \end{bmatrix}. \tag{7}$$

Let us consider two matrices $\boldsymbol{A}_1 \in \mathbb{R}^n \times m$ and $\boldsymbol{B}_1 \in \mathbb{R}^{p \times q}$, the kroneker product $\boldsymbol{A}_1 \otimes \boldsymbol{B}_1$ is defined as

$$\boldsymbol{A}_1 \otimes \boldsymbol{B}_1 = \begin{bmatrix} a_{11}\boldsymbol{B}_1 & \dots & a_{1m}\boldsymbol{B}_1 \\ \vdots & & \vdots \\ a_{n1}\boldsymbol{B}_1 & \dots & a_{nm}\boldsymbol{B}_1 \end{bmatrix} \in \mathbb{R}^{np \times mq}.$$

3. System description and modeling

This section begins with an exposition of the system description, followed by a detailed overview of the experimental setup.

3.1. System description

The system under study is a well-known academic body referred to as Windsor body (Good and Garry 15, Pavia et al. 30). A back side view is showed in Figure 1. The system is sketched in Figure 2. The active control strategy presented here has been first tested on the same model without wheels. We only present here the case with wheels, which corresponds to the higher complexity case. Pressure taps are installed on the body as well as four rigid flaps at the base. The presence of the wheels introduces underflow perturbations, disrupting the flow and creating a momentum deficit in the wake. This deficit fosters interactions between the wheels and the surrounding airflow, significantly impacting the overall aerodynamic performance of the vehicle. This phenomenon is known as wheel-wake interaction and has been extensively addressed by Bao et al. 3. The characteristic lengths of our model are detailed in the Table 1.

Figure 1: Windsor body equipped with the four actuated flaps on the rear.

In Figure 3, the system is presented from both lateral-back (left-hand side) and back views. The origin O (in green) of the coordinate system (x, y, z) is located at the center of the body's base, with x, y and z defined, respectively, along the streamwise, span-wise and floor-normal directions. In the lateral-back view, the focus is on the four rigid flaps and their displacement angle θ_i. In what follows, indices 1, 2, 3 and 4 correspond respectively to the left, right, top and bottom flap. These latter serve as the system inputs $\boldsymbol{u}$ and have the capability to move

Parameter	Symbol	Value	Unit
Height	H	0.289	m
Width	W	0.389	m
Base Surface	S_b	0.112	m^2
Length	L	1.037	m
Ground Clearance	G	0.05	m
Wheel width	w	0.055	m
Wheel diameter	D_w	0.150	m
Flap Length	δ	0.05	m
Flap Amplitude	θ	± 7	*degrees*

Table 1: Parameters of the model under study.

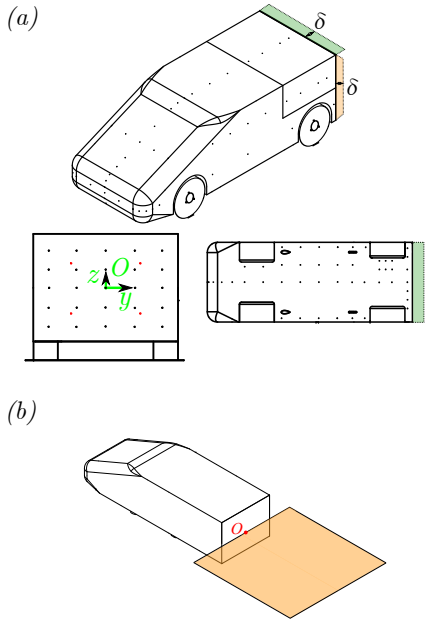

Figure 2: System under study. (a) Some views of the model under study. (b) Field of view of the PIV measurements. Adapted from Bao 2.

inward ($\theta_i > 0$) or outward ($\theta_i < 0$) with an angular velocity of $\sim 10\ deg/s$. They can oscillate within a maximum amplitude of $\pm 7°$. Shifting to the back view, attention is drawn to the four pressure taps p_i, $i = 1, \ldots, 4$ (highlighted in red) that play a crucial role in computing the system outputs $\boldsymbol{y}$. The position of these pressure taps, $dy \simeq 0.47\ W$ and $dz \simeq 0.44\ H$, has been chosen since it gives a precise information about the large scale properties of the base pressure spatial distribution at the scale of the body (Khan et al. 24, Fan et al. 13, Bonnavion et al. 5).

The body is fixed on a turntable to enable the alteration of the velocity direction experienced by the car (Fig. 4). The yaw angle β is considered positive in the direction of the arrow, *i.e.*, the system nose pointing towards the right-hand side. The zero yaw condition is measured at the beginning of each testing campaign and it corresponds to the Windsor body's symmetry plane aligned with the flow's direction.

A vertically moving upstream grid is used to induce underflow perturbations. The grid measures $0.08\,m$ in height and $1.5\,m$ in width. It is designed with a porosity of approximately 50%. The latter allows for controlled perturbations in the flow while

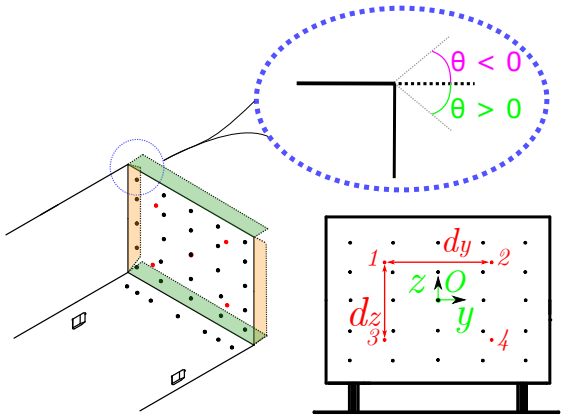

Figure 3: Control system schematisation. In orange and green the four rigid flaps, θ being the flap's displacement. The red pressure taps are the ones used for the system's outputs

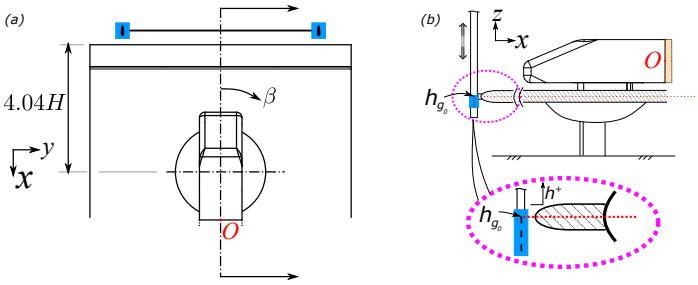

Figure 4: Top and side views of the system under study. Perturbations schematisation. (a) Yaw angle schematisation. (b) Underflow perturbation schematisation

minimizing excessive pressure loss in the downstream region (based on Idelchik and Meury 20, Castelain et al. 7). The reference grid height, denoted as h_{g_0}, is defined as the level at which the top of the grid aligns with the symmetry plane of the raised floor. The maximum grid height is $h_g = 100\,mm$ while the minimum is $h_g = -200\,mm$. The latter being considered as the non perturbed case in which we can retrieve the reference model case (Bao et al. 3, Pavia et al. 30, Varney et al. 36)

3.2. Experiment setup

The experimental tests have been conducted in the S620 ENSMA closed-loop subsonic wind tunnel (Figure 5). The test section dimensions are $2.4\,m$ in height and $2.6\,m$ in width, with a length $L = 5\,m$. The maximum wind speed achievable in the test section is $V = 60\,m/s$. The retained testing speed is $V_\infty = 30\,m/s$ which corresponds to a Reynolds number $Re_H = V_\infty H/\nu \simeq 6.10^5$ based on the model's base height (ν is the kinematic viscosity of air). This value is large enough to provide all the relevant wake physics for this turbulent flow because all boundary layers are triggered to turbulence and the flow separates at the sharp trailing edges of the flaps surrounding the base. The grids, upstream of the test section, reduce the turbulence intensity, which is of the order of 0.3 %, as well as the spatial inhomogeneity that is lower than 0.5 %.

The test section is depicted in Figure 6. The flow characteristics are measured via a Prandtl antennae and a temperature

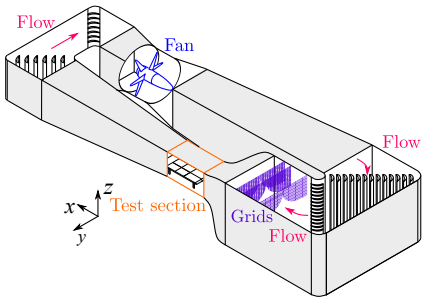

Figure 5: S620 Wind tunnel schematisation, adapted from Bao 2.

sensor. A raised floor is used to simulate the ground with the aim to control the boundary layer characteristics upstream of the model in unperturbed conditions. The boundary layer displacement thickness is approximately 2% of the model ground clearance (G). The dimensions of the floor are $\simeq 2.38\,m$ in width with a length of $\simeq 3.5\,m$. The latter features a profiled leading edge, a flat plate and a rear flap. The rear flap is used to regulate the flow above and below the raised floor by varying the angle α. Inside the flat plate there is a turntable, which allows to rotate the model to simulate the yaw angle (β in Figure 4) with an angular velocity of $\sim 2\ deg/s$. Upstream the raised floor, as discussed in section 3.1, a movable grid can be adjusted vertically to introduce perturbations in the model underflow.

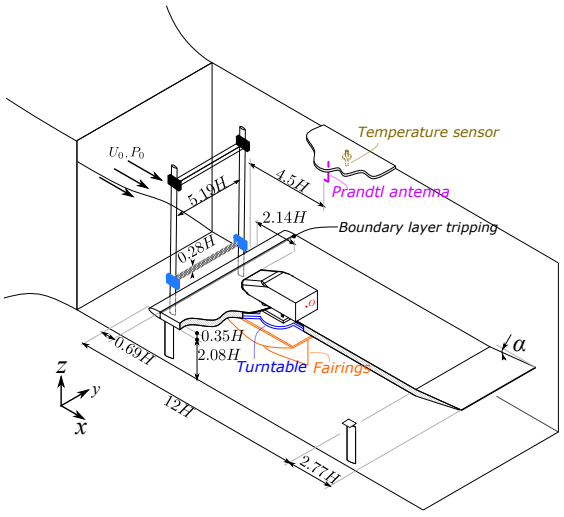

Figure 6: Test section and setup schematisation, adapted from Bao 2.

The analysis in our study concentrates on the so called base pressure drag coefficient C_b, with particular emphasis on the pressure data obtained from 25 pressure taps situated at the base of the vehicle (see Eq. (9)). The data collected from these pressure taps are used as a key source of information for our analysis on the overall aerodynamic performance of the vehicle. Furthermore, some Particle Image Velocimetry (PIV) measurements are performed to validate the effectiveness of the flaps on the vehicle's wake. The time-averaged and long-timescale pressure measurements are performed with two 64-channel ESP-DTC pressure scanners which are linked to the pressure taps via $1mm$ diameter vinyl tubes that measure $78cm$ in length. The accuracy of the scanner stands in $\pm 1.5Pa$ range and the acquisition are conducted at a sampling rate of $100Hz$. In order to perform comparison between different tests we will rely on a dimensionless parameter that is the pressure coefficient, which is defined as:

$$C_{p_i} = \frac{p_i - p_\infty}{Q}, \tag{8}$$

where p_i is the static pressure measured on the i^{th} pressure tap, p_∞ is the static pressure upstream measured with the Prandtl antenna depicted in Figure 6 and $Q = \frac{1}{2}\rho_\infty V_\infty^2$ corresponds to the dynamic pressure with ρ_∞ being the fluid mass density and V_∞ being the free-stream velocity. According to the definition in (8), the base pressure drag is quantified with the space averaged base pressure coefficient:

$$C_b = -\frac{\int_{S_b} C_p\, ds}{S_b}, \tag{9}$$

where S_b represent the model's base surface.

Experiments conducted in the wind tunnel, with the flaps set to a neutral position (zero angle), revealed a significant reliance of horizontal and vertical pressure coefficient gradients on the values of β and h_g. Furthermore, we observed a direct correlation between the average pressure coefficient at the rear of the vehicle and these two variables. These observations enabled the formulation of the output vector $\boldsymbol{y}$, which is expressed as a function of the four pressure coefficients obtained from the four sensors located at the rear of the body. The first two components of vector $\boldsymbol{y}$ represent the horizontal and vertical pressure coefficients gradients, respectively. The third component provides a representation of the average pressure coefficient at the rear of the body. The output vector $\boldsymbol{y} \in \mathbb{R}^3$ is specified as

$$\boldsymbol{y} = \begin{bmatrix} C_{p_1} - C_{p_2} + C_{p_3} - C_{p_4} \\ C_{p_1} + C_{p_2} - C_{p_3} - C_{p_4} \\ C_{p_1} + C_{p_2} + C_{p_3} + C_{p_4} \end{bmatrix}.$$

Here C_{p_i}, $i = 1, \ldots, 4$ are computed from (8) using the four pressure taps p_i (see fig. 3).

Concerning the velocity measurements behind the body, we used a two dimensions - two components Particle Image Velocimetry method (2D-2C PIV). In this respect, only one two-dimensional field of view is considered as schematised in Figure 2(b). Particles, which have a diameter $d \simeq 1\ \mu m$, are injected in the flow, then they are enlightened with a laser and a pair of images is taken with a camera in order to follow the particle displacement and calculate the speed and direction of the flow. In our specific case, the plane measures $2.6H$ and $1.7H$, respectively in width and length. It coincides with the horizontal symmetry plane ($z/H = 0$) and allows to compute the stream-wise u_x and horizontal u_y velocity components. For each test case we captured 1200 independent pair of images, at a sample rate of $4Hz$, which have been processed with an interrogation window of 16 x 16 pixels and an overlap of 50%.

4. Control law definition

Experiments conducted in the wind tunnel revealed that, for each specific value of the perturbation $[\beta,\ h_g]^\top$, the system can

be modeling by a discrete-time LTI model with a state realization ($\boldsymbol{A}$, $\boldsymbol{B}$, $\boldsymbol{C}$, $\boldsymbol{D}$) that depends on the perturbation. On a vehicle in a real-word environment, measuring the perturbation necessitates heavy and complex instrumentation, such as a multihole probe, which is impractical for a production vehicle. This finding reinforces the idea that, for control purposes, the system can be more suitably represented by a Linear Time-Varying (LTV) model, where variations are not known *a priori*. This LTV system can then be controlled either through robust control, ensuring the stability of the closed-loop despite parametric variations (Zhou and Doyle 40), or by employing an adaptive control law in conjunction with a recursive estimator (Åström and Wittenmark 1). In applications where parameter variations are significant, the adaptive approach is often favored to alleviate the conservatism inherent in the robust approach. Therefore, we address the control problem introduced previously by considering the output regulation problem of a Linear Time-Varying system. In order to reach this goal, we introduce an adaptive subspace-based predictive control procedure.

4.1. Unbiased Adaptive Subspace-based Predictive Control

The concept behind predictive control is to compute, at each time step, an optimal control sequence over a horizon ℓ that minimizes a specific cost function while adhering to specific constraints. Broadly speaking, by considering herein input saturations as constraints only, we aim at determining the sequence $\boldsymbol{U}_{k,\ell,1}$ that minimizes

$$\arg\min_{\boldsymbol{U}_{k,\ell,1}} \left\|\hat{\boldsymbol{Y}}_{k,\ell,1} - \boldsymbol{Y}_r\right\|_{\boldsymbol{Q}}^2 + \left\|\boldsymbol{U}_{k,\ell,1}\right\|_{\boldsymbol{\mathcal{R}}}^2, \tag{10a}$$

$$\text{s.t.} \quad \boldsymbol{U}_{k,\ell,1}^{(i)} \in \boldsymbol{\mathcal{U}}, \quad i = 1, \ldots, \ell, \tag{10b}$$

where, according to the notations introduced in Section 2, $\boldsymbol{U}_{k,\ell,1} \in \mathbb{R}^{\ell n_u \times 1}$ and $\hat{\boldsymbol{Y}}_{k,\ell,1} \in \mathbb{R}^{\ell n_y \times 1}$ denote vectors made by stacking the input sequence $(\boldsymbol{u}(i))_{i=k}^{k+\ell-1}$ and the predicted output sequence $(\hat{\boldsymbol{y}}(i))_{i=k}^{k+\ell-1}$, respectively whereas $\boldsymbol{Y}_r \in \mathbb{R}^{\ell n_y \times 1}$ stands for

$$\boldsymbol{Y}_r = \begin{bmatrix} \boldsymbol{y}_r(k) \\ \vdots \\ \boldsymbol{y}_r(k+\ell-1) \end{bmatrix}. \tag{11}$$

$\boldsymbol{Y}_r$ is the reference trajectory over the prediction horizon. $\boldsymbol{Q} \in \mathbb{R}^{n_y \ell \times n_y \ell}$ and $\boldsymbol{\mathcal{R}} \in \mathbb{R}^{n_u \ell \times n_u \ell}$ are user-defined output and input error penalizing positive definite matrices. They are tuned based on a trade-off between the degree of importance of each of the outputs and inputs terms. $\boldsymbol{\mathcal{U}}$ is the polytope defining the applicable lower and upper boundaries of the system input. In order to determine the sequence $\boldsymbol{U}_{k,\ell,1}$ minimizing (10), it is crucial to establish the set of equations relating $\hat{\boldsymbol{Y}}_{k,\ell,1}$ and $\boldsymbol{U}_{k,\ell,1}$. When Linear Time Invariant systems are considered, several solutions have been developed in the literature. Among the solutions dedicated to LTI systems, the behavior of which can be described by the following innovation state space representation

$$\boldsymbol{x}(k+1) = \boldsymbol{A}\boldsymbol{x}(k) + \boldsymbol{B}\boldsymbol{u}(k) + \boldsymbol{K}\boldsymbol{e}(k), \tag{12a}$$

$$\boldsymbol{y}(k) = \boldsymbol{C}\boldsymbol{x}(k) + \boldsymbol{D}\boldsymbol{u}(k) + \boldsymbol{e}(k), \tag{12b}$$

where $\boldsymbol{e}(k) \in \mathbb{R}^{n_y}$ is the innovation vector and $\boldsymbol{K}$ is the Kalman gain, a specific attention is paid herein to the output predictors generated via the subspace model learning solutions. As explained in (Overchee and Moor 29) and recalled in Appendix A , assuming that

Assumption 1. *The innovation sequence $\boldsymbol{e}(k)$ is an ergodic zero-mean white noise sequence with covarianvce matrix $\mathbf{R}_e$,*

Assumption 2. *The pair $(\boldsymbol{A}, \boldsymbol{C})$ is observable and the pair $(\boldsymbol{A}, [\boldsymbol{B}, \boldsymbol{K}\boldsymbol{R}_e^{1/2}])$ is reachable,*

it can be straightforwardly shown that (see Appendix A)

$$\begin{aligned} \boldsymbol{Y}_{i,\ell,\bar{N}}^f &= \boldsymbol{\Gamma}_\ell(\boldsymbol{A}, \boldsymbol{C})\boldsymbol{\mathcal{K}}\boldsymbol{W}_{i-\rho,\rho,\bar{N}}^p + \boldsymbol{H}_\ell(\boldsymbol{A}, \boldsymbol{B}, \boldsymbol{C}, \boldsymbol{D})\boldsymbol{U}_{i,\ell,\bar{N}}^f \\ &\quad + \boldsymbol{H}_\ell(\boldsymbol{A}, \boldsymbol{K}, \boldsymbol{C}, \boldsymbol{I})\boldsymbol{E}_{i,\ell,\bar{N}}^f, \end{aligned} \tag{13}$$

or, more compactly,

$$\boldsymbol{Y}_{i,\ell,\bar{N}}^f = \boldsymbol{L}_w \boldsymbol{W}_{i-\rho,\rho,\bar{N}}^p + \boldsymbol{L}_u \boldsymbol{U}_{i,\ell,\bar{N}}^f + \boldsymbol{L}_e \boldsymbol{E}_{i,\ell,\bar{N}}^f, \tag{14}$$

where the matrices $\boldsymbol{L}_w$, $\boldsymbol{L}_u$ and $\boldsymbol{L}_e$ are made of specific combinations of the state space matrices $\boldsymbol{A}$, $\boldsymbol{B}$, $\boldsymbol{C}$, $\boldsymbol{D}$ and $\boldsymbol{K}$, thus are unknown *a priori*. Under open loop conditions, *i.e.*, when the noise sequence $\boldsymbol{E}_{i,\ell,\bar{N}}^f$ is uncorrelated with the both past and future input and output data, the unknown matrices $\boldsymbol{L}_w$ and $\boldsymbol{L}_u$ can be estimated accurately by minimizing the cost function

$$\min_{\boldsymbol{L}} \left\| \boldsymbol{Y}_{i,\ell,\bar{N}}^f - \boldsymbol{L} \begin{bmatrix} \boldsymbol{W}_{i-\rho,\rho,\bar{N}}^p \\ \boldsymbol{U}_{i,\ell,\bar{N}}^f \end{bmatrix} \right\|_F^2, \tag{15}$$

with $\boldsymbol{L} = \begin{bmatrix} \boldsymbol{L_W} & \boldsymbol{L_u} \end{bmatrix}$. Given these consistent estimates $\hat{\boldsymbol{L}}_w$ and $\hat{\boldsymbol{L}}_u$, $\hat{\boldsymbol{Y}}_{k,\ell,1}$ can be expressed as

$$\hat{\boldsymbol{Y}}_{k,\ell,1} = \hat{\boldsymbol{L}}_W \boldsymbol{W}_{k-\rho,\rho,1}^p + \hat{\boldsymbol{L}}_u \boldsymbol{U}_{k,\ell,1}^f. \tag{16}$$

Including (16) into (10) results in

$$\arg\min_{\boldsymbol{U}_{k,\ell,1}^f} \left\| \hat{\boldsymbol{L}}_{\boldsymbol{W}} \boldsymbol{W}_{k-\rho,\rho,1}^p + \hat{\boldsymbol{L}}_{\boldsymbol{u}} \boldsymbol{U}_{k,\ell,1}^f - \boldsymbol{Y}_r \right\|_{\boldsymbol{Q}}^2 + \left\| \boldsymbol{U}_{k,\ell,1}^f \right\|_{\boldsymbol{\mathcal{R}}}^2 \tag{17a}$$

$$\text{s.t.} \quad \boldsymbol{U}_{k,\ell,1}^{f(i)} \in \boldsymbol{\mathcal{U}}, \quad i = 1, \ldots, \ell. \tag{17b}$$

The control law applied to the system is given by the first n_u rows of $\boldsymbol{U}_{k,\ell,1}^f$, *i.e.* $\boldsymbol{u}(k)$. When data is acquired under closed loop practical conditions, the noise sequence is correlated with the output data, causing the former estimators $\hat{\boldsymbol{L}}_w$ and $\hat{\boldsymbol{L}}_u$ to become biased. To address this issue, several solutions have been proposed in the literature (Verhaegen and Verdult 37, Jansson 21, Chiuso 10). These include the introduction of an instrumental variable or the implementation of an initial step for innovation estimation. In this paper, the latter approach is employed. As suggested in (Mercere et al. 28), we can see that

$$\boldsymbol{Y}_{i,1,\bar{N}}^f = \boldsymbol{C}\boldsymbol{\mathcal{K}}\boldsymbol{W}_{i-\rho,\rho,\bar{N}}^p + \boldsymbol{D}\boldsymbol{U}_{i,1,\bar{N}}^f + \boldsymbol{E}_{i,1,\bar{N}}^f, \tag{18}$$

by just looking at the first n_y rows of Eq. (14). Then, if $\boldsymbol{D} = \boldsymbol{0}$ and with Assumption 1, we can prove that

$$\lim_{\bar{N}\to\infty} \frac{1}{\bar{N}} \boldsymbol{E}^f_{i,1,\bar{N}} \boldsymbol{W}^{p\top}_{i-\rho,\rho,\bar{N}} = \boldsymbol{0}.$$

It follows that the optimal prediction of $\boldsymbol{Y}^f_{i,1,\bar{N}}$ in the least-squares sense is given by

$$\hat{\boldsymbol{Y}}^f_{i,1,\bar{N}} = \boldsymbol{Y}^f_{i,1,\bar{N}} \left(\boldsymbol{W}^p_{i-\rho,\rho,\bar{N}}\right)^{\dagger} \boldsymbol{W}^p_{i-\rho,\rho,\bar{N}}. \tag{19}$$

An optimal estimate, in the least squares sense, of $\boldsymbol{E}^f_{i,1,\bar{N}}$ is obtained as follows

$$\hat{\boldsymbol{E}}^f_{i,1,\bar{N}} = \boldsymbol{Y}^f_{i,1,\bar{N}} - \hat{\boldsymbol{Y}}^f_{i,1,\bar{N}}. \tag{20}$$

Once $\hat{\boldsymbol{E}}^f_{i,1,\bar{N}}$ is available, from Eq. (14), a linear predictor of $\boldsymbol{Y}^f_{i,\ell,\bar{N}}$ is of the form

$$\hat{\boldsymbol{Y}}^f_{i,\ell,\bar{N}} = \hat{\boldsymbol{L}}_W \boldsymbol{W}^p_{i-\rho,\rho,\bar{N}} + \hat{\boldsymbol{L}}_u \boldsymbol{U}^f_{i,\ell,\bar{N}} + \hat{\boldsymbol{L}}_e \hat{\boldsymbol{E}}^f_{i,\ell,\bar{N}}. \tag{21}$$

The least squares prediction $\hat{\boldsymbol{Y}}^f_{i,\ell,\bar{N}}$ of $\boldsymbol{Y}^f_{i,\ell,\bar{N}}$ is now the solution to:

$$\min_{\boldsymbol{L}} \left\| \boldsymbol{Y}^f_{i,\ell,\bar{N}} - \hat{\boldsymbol{L}} \begin{bmatrix} \boldsymbol{W}^p_{i-\rho,\rho,\bar{N}} \\ \boldsymbol{U}^f_{i,\ell,\bar{N}} \\ \hat{\boldsymbol{E}}^f_{i,\ell,\bar{N}} \end{bmatrix} \right\|^2_F, \tag{22}$$

where $\hat{\boldsymbol{L}}$ is now given by $\hat{\boldsymbol{L}} = \begin{bmatrix} \hat{\boldsymbol{L}}_W & \hat{\boldsymbol{L}}_u & \hat{\boldsymbol{L}}_e \end{bmatrix}$. We now have a method for estimating the matrices $\boldsymbol{L_u}$ and $\boldsymbol{L_w}$ in a closed loop without bias. In the following section, we present the online implementation of this method.

4.2. Recursive formulation

Despite the theoretical efficiency of the model learning solution introduced so far, its use on an embedded system can be computationally cumbersome. To overcome this challenge, we suggest implementing it online. To reach this goal, we refer to the temporal ordering shown in Figure 7 and define three distinct discrete time intervals such as

$$\begin{aligned} \boldsymbol{T}_1 &= [k-\rho-\ell,\ \ldots,\ k-\ell-1], \\ \boldsymbol{T}_2 &= [k-\ell,\ \ldots,\ k-1], \\ \boldsymbol{T}_3 &= [k,\ \ldots,\ k+\ell-1]. \end{aligned}$$

At time k, we have ℓ pairs of inputs/outputs denoted as $\boldsymbol{W}^p_{k-\ell,\ell,1}$, collected over the time interval $\boldsymbol{T}_2$.

$$\boldsymbol{W}^p_{k-\ell,\ell,1} = \begin{bmatrix} \boldsymbol{Y}_{k-\ell,\ell,1} \\ \boldsymbol{U}_{k-\ell,\ell,1} \end{bmatrix}. \tag{23}$$

Equation (19) can be rewritten over $\boldsymbol{T}_2$ by considering only the first column of the Hankel matrices:

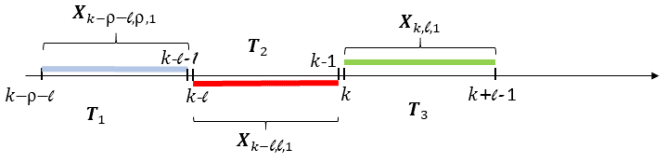

Figure 7: Time ordering.

$$\hat{\boldsymbol{Y}}^f_{k,1,1} = \boldsymbol{Y}^f_{k,1,1} \left(\boldsymbol{W}^p_{k-\ell,\ell,1}\right)^{\dagger} \boldsymbol{W}^p_{k-\ell,\ell,1}. \tag{24}$$

The solution to Eq. (24) can be found using the recursive form of the least-squares Algorithm 1, as outlined in the following steps. When parameters change gradually over time, a common method for adapting recursive linear least squares algorithms to track these slow variations involves introducing a forgetting factor. This approach works by reducing the weight of older measurements, effectively allowing them to be discarded when they no longer represent current conditions.

Algorithm 1 Recursive estimation of $\hat{\boldsymbol{y}}(k)$

Choose $\boldsymbol{P}_e(0)$ and λ_e suitably
for $k = \rho + \ell + 1, \cdots$ **do**
  Measure $\boldsymbol{y}(k)$
  $\boldsymbol{\xi}(k-1) = \boldsymbol{W}^{p\top}_{k-\ell,\ell,1} \boldsymbol{P}_e(k-1)$
  $\boldsymbol{Z}_e(k) = \left(\lambda_e^{-1} + \boldsymbol{\xi}(k-1)\boldsymbol{W}^p_{k-\ell,\ell,1}\right)^{-1} \boldsymbol{\xi}(k-1)$
  $\boldsymbol{P}_e(k) = \boldsymbol{P}_e(k-1) - \boldsymbol{\xi}(k-1)^{\top} \boldsymbol{Z}_e(k)$
  $\boldsymbol{\Gamma}_e(k) = \boldsymbol{\Gamma}_e(k-1) + \left(\boldsymbol{y}(k) - \boldsymbol{\Gamma}_e(k-1)\boldsymbol{W}^p_{k-\ell,\ell,1}\right) \boldsymbol{Z}_e(k)$
  $\hat{\boldsymbol{y}}(k) = \boldsymbol{\Gamma}_e(k) \boldsymbol{W}^p_{k-\ell,\ell,1}$
end for

Given an estimate of $\hat{\boldsymbol{Y}}^f_{k,1,1} = \hat{\boldsymbol{y}}(k)$, we can determine the innovation $\hat{\boldsymbol{e}}(k)$ as follows

$$\hat{\boldsymbol{e}}(k) = \boldsymbol{y}(k) - \hat{\boldsymbol{y}}(k). \tag{25}$$

Then $\hat{\boldsymbol{E}}^f_{k-\ell,\ell,1}$ is updated as follows

$$\hat{\boldsymbol{E}}^f_{k-\ell+1,\ell,1} = \begin{bmatrix} \hat{\boldsymbol{e}}(k-\ell+1) \\ \vdots \\ \hat{\boldsymbol{e}}(k) \end{bmatrix}. \tag{26}$$

Using Eq. (26), we can now update the estimates $\hat{\boldsymbol{L}}_w$, $\hat{\boldsymbol{L}}_u$ and $\hat{\boldsymbol{L}}_e$ over the time intervals $\boldsymbol{T}_1$ and $\boldsymbol{T}_2$. To proceed, let us focus on the first column of Eq. (21)

$$\hat{\boldsymbol{Y}}^f_{k-\ell+1,\ell,1} = \hat{\boldsymbol{L}}_w \boldsymbol{W}^p_{k-\rho-\ell,\rho,1} + \hat{\boldsymbol{L}}_u \boldsymbol{U}^f_{k-\ell,\ell,1} + \hat{\boldsymbol{L}}_e \hat{\boldsymbol{E}}^f_{k-\ell+1,\ell,1}, \tag{27}$$

and consider the stack of data

$$\boldsymbol{\xi}_y(k) = \begin{bmatrix} \boldsymbol{W}^p_{k-\rho-\ell,\rho,1} \\ \boldsymbol{U}^f_{k-\ell,\ell,1} \\ \hat{\boldsymbol{E}}^f_{k-\ell+1,\ell,1} \end{bmatrix}.$$

Eq. (27) can be rewritten as follows

$$\hat{\boldsymbol{Y}}^f_{k-\ell+1,\ell,1} = \hat{\boldsymbol{L}}\boldsymbol{\xi}_y(k), \tag{28}$$

where $\hat{\boldsymbol{L}} = \begin{bmatrix}\hat{\boldsymbol{L}}_w & \hat{\boldsymbol{L}}_w & \hat{\boldsymbol{L}}_e\end{bmatrix}$. The update of $\hat{\boldsymbol{L}}_w$, $\hat{\boldsymbol{L}}_u$ and $\hat{\boldsymbol{L}}_e$ at time k is provided by the recursive least squares algorithm 2 where

$$\begin{aligned}\hat{\boldsymbol{L}}_W &= \hat{\boldsymbol{L}}(:, 1:(n_u+n_y)\rho),\\ \hat{\boldsymbol{L}}_u &= \hat{\boldsymbol{L}}(:, (n_u+n_y)\rho+1:(n_u+n_y)\rho+n_u\ell),\\ \hat{\boldsymbol{L}}_e &= \hat{\boldsymbol{L}}(:, (n_u+n_y)\rho+n_u\ell:end),\end{aligned}$$

and λ_y a forgetting factor. We now have unbiased estimates $\hat{\boldsymbol{L}}_w$ and $\hat{\boldsymbol{L}}_u$ which can be used to solve (17) over the time interval $\boldsymbol{T}_3$. Indeed, over $\boldsymbol{T}_3$, the optimal prediction of $\boldsymbol{Y}^f_{k,\ell,1}$ in the least-squares sense is given by

$$\hat{\boldsymbol{Y}}^f_{k,\ell,1} = \hat{\boldsymbol{L}}_w\boldsymbol{W}^p_{k-\rho,\rho,1} + \hat{\boldsymbol{L}}_u\boldsymbol{U}^f_{k,\ell,1}, \tag{29}$$

requiring only the estimates of the matrices $\boldsymbol{L}_w$ and $\boldsymbol{L}_u$.

Algorithm 2 Recursive estimation of $\hat{\boldsymbol{L}}$

1: Choose $\boldsymbol{P}_y(0)$ and λ_y suitably
2: **for** $k = \rho+\ell+1, \cdots$ **do**
3: Estimate $\hat{\boldsymbol{e}}(k)$ from Alggorithm 1 and update $\boldsymbol{\xi}_y(k)$
4: $\boldsymbol{Z}_y(k) = \left(\lambda_y^{-1} + \boldsymbol{\xi}_y^\top(k)\boldsymbol{P}_y(k-1)\boldsymbol{\xi}_y(k)\right)^{-1}\boldsymbol{\xi}_y^\top(k)\boldsymbol{P}_y(k-1)$
5: $\boldsymbol{P}_y(k) = \boldsymbol{P}_y(k-1) - \boldsymbol{P}_y(k-1)\boldsymbol{\xi}_y(k)\boldsymbol{Z}_y(k)$
6: $\hat{\boldsymbol{L}}(k) = \hat{\boldsymbol{L}}(k-1) + \left(\boldsymbol{Y}_{k-\ell+1,\ell,1} - \hat{\boldsymbol{L}}(k-1)\boldsymbol{\xi}_y(k)\right)\boldsymbol{Z}_y(k)$
7: **end for**

4.3. Explicit formulation of the controller

The command $\boldsymbol{u}(k)$, as the solution of optimization problem (17), does not solve the regulation problem exactly in its current form. Before providing an explicit form of the control, it is necessary to incorporate integral action to achieve precise regulation. Incorporating an integrator into the control loop enables the precise tracking of an output reference with zero offset. To introduce integral action into the predictive controller based on subspace matrices, we adopt the approach outlined in Huang and Kadali 18, Chapter 7.2.1, focusing on the subspace equation:

$$\Delta\hat{\boldsymbol{Y}}^f_{k,\ell,1} = \hat{\boldsymbol{L}}_W\Delta\boldsymbol{W}^p_{k-\rho,\rho,1} + \hat{\boldsymbol{L}}_u\Delta\boldsymbol{U}^f_{k,\ell,1}. \tag{30}$$

By performing a direct computation using Eq. (30), we arrive at:

$$\hat{\boldsymbol{Y}}^f_{k,\ell,1} = \boldsymbol{Y}_k + \hat{\boldsymbol{L}}_{W_I}\Delta\boldsymbol{W}^p_{k-\rho,\rho,1} + \hat{\boldsymbol{L}}_{u_I}\Delta\boldsymbol{U}^f_{k,\ell,1}, \tag{31}$$

with $\hat{\boldsymbol{L}}_{W_I} = \boldsymbol{S}_{\ell,n_y}\hat{\boldsymbol{L}}_W$, $\hat{\boldsymbol{L}}_{u_I} = \boldsymbol{S}_{\ell,n_y}\hat{\boldsymbol{L}}_u$ and $\boldsymbol{Y}_k = \mathbb{1}_{\ell,n_y}\otimes\boldsymbol{y}(k)$. In the formulation of the optimization problem (17), we will used the predictor (31) instead of (29). The formulation of Problem (17) can now be articulated as

$$\arg\min_{\Delta\boldsymbol{U}^f_{k,\ell,1}}\left(\frac{1}{2}\Delta\boldsymbol{U}^{f\top}_{k,\ell,1}\boldsymbol{E}\Delta\boldsymbol{U}^f_{k,\ell,1} + \Delta\boldsymbol{U}^{f\top}_{k,\ell,1}\boldsymbol{F}\right), \tag{32a}$$

$$\text{s.t.}\quad \boldsymbol{M}\Delta\boldsymbol{U}^f_{k,\ell,1} \le \boldsymbol{\gamma}, \tag{32b}$$

where

$$\begin{aligned}\boldsymbol{E} &= \mathcal{R} + \hat{\boldsymbol{L}}^\top_{\boldsymbol{u_I}}\mathcal{Q}\hat{\boldsymbol{L}}_{\boldsymbol{u_I}},\\ \boldsymbol{F} &= -\hat{\boldsymbol{L}}^\top_{\boldsymbol{u_I}}\mathcal{Q}\left(\boldsymbol{Y}_r - \hat{\boldsymbol{L}}_{\boldsymbol{w_I}}\Delta\boldsymbol{W}^p_{k-\rho,\rho,1} - \boldsymbol{Y}_k\right),\\ \boldsymbol{M} &= \begin{bmatrix}-\boldsymbol{S}_{\ell,n_u}\\ \boldsymbol{S}_{\ell,n_u}\end{bmatrix},\\ \boldsymbol{\gamma} &= \begin{bmatrix}\mathbf{1}_{\ell,n_y}\otimes\boldsymbol{u}(k-1) - \boldsymbol{U}_{min}\\ \boldsymbol{U}_{max} - \mathbf{1}_{\ell,n_y}\otimes\boldsymbol{u}(k-1)\end{bmatrix}.\end{aligned}$$

The necessary Kuhn-Tucker conditions for this optimization problem are

$$\boldsymbol{E}\Delta\boldsymbol{U}^f_{k,\ell,1} + \boldsymbol{F} + \sum_{i\in W_a}\lambda^{(i)}\boldsymbol{M}^{(i)\top} = 0, \tag{33a}$$

$$\boldsymbol{M}^{(i)}\Delta\boldsymbol{U}^f_{k,\ell,1} - \gamma^{(i)} = 0, \quad i\in\boldsymbol{W}_a, \tag{33b}$$

$$\boldsymbol{M}^{(i)}\Delta\boldsymbol{U}^f_{k,\ell,1} - \gamma^{(i)} \le 0, \quad i\notin\boldsymbol{W}_a, \tag{33c}$$

$$\lambda^{(i)} \ge 0, \quad i\in\boldsymbol{W}_a, \tag{33d}$$

$$\lambda^{(i)} = 0, \quad i\notin\boldsymbol{W}_a, \tag{33e}$$

where $\boldsymbol{\lambda}\in\mathbb{R}^{2\ell n_u}$ represents the vector of Lagrange multipliers and $\boldsymbol{W}_a$ the index set of active constraints. If $\boldsymbol{W}_a$ were known, it is well-known that the optimal solution would be given by

$$\Delta\boldsymbol{U}^f_{k,\ell,1} = -\boldsymbol{E}^{-1}\left(\boldsymbol{F} + \boldsymbol{M}_a^\top\boldsymbol{\lambda}_a\right), \tag{34}$$

where $\boldsymbol{M}_a$ (resp. $\boldsymbol{\lambda}_a$) contains the rows of $\boldsymbol{M}$ (resp. $\boldsymbol{\lambda}$) with indices in $\boldsymbol{W}_a$. The challenge lies in the impossibility of *a priori* knowledge regarding the active or inactive status of constraints. This gives rise to the well-known issue of determining online the set of active constraints $\boldsymbol{W}_a$. In the general case, solving this problem is not straightforward. However, its complexity can be mitigated when the constraints arise from saturations, as in our case, because the active constraints are linearly independent, and their number is less than or equal to the number of decision variables. If we suppose that there exists an optimal input sequence $\Delta\boldsymbol{U}^f_{k,\ell,1}$ such that $\boldsymbol{M}\Delta\boldsymbol{U}^f_{k,\ell,1} < \boldsymbol{\gamma}$, the problem (32) is equivalent to

$$\max_{\lambda\ge0}\min_{\Delta\boldsymbol{U}^f_{k,\ell,1}}\left(\frac{1}{2}\Delta\boldsymbol{U}^{f\top}_{k,\ell,1}\boldsymbol{E}\Delta\boldsymbol{U}^f_{k,\ell,1} + \Delta\boldsymbol{U}^{f\top}_{k,\ell,1}\boldsymbol{F} + \lambda^\top\left(\boldsymbol{M}\Delta\boldsymbol{U}^f_{k,\ell,1} - \boldsymbol{\gamma}\right)\right).$$

The minimization over $\boldsymbol{U}^f_{k,\ell,1}$ is unconstrained and the solution is given by

$$\Delta\boldsymbol{U}^f_{k,\ell,1} = -\boldsymbol{E}^{-1}\left(\boldsymbol{F} + \boldsymbol{M}^\top\boldsymbol{\lambda}\right), \tag{35}$$

leading to the formulation of the dual problem

$$\arg\min_{\lambda\ge0}\left(\frac{1}{2}\lambda^\top\boldsymbol{G}\lambda + \lambda^\top\boldsymbol{\Omega}\right), \tag{36}$$

with $\boldsymbol{G} = \boldsymbol{M}\boldsymbol{E}^{-1}\boldsymbol{M}^\top$ and $\boldsymbol{\Omega} = \boldsymbol{\gamma} + \boldsymbol{M}\boldsymbol{E}^{-1}\boldsymbol{F}$. It is important to observe that $\lambda^{(i)} = 0$ when the i^{th} inequality is inactive. Problem (36) is much easier to solve than the original problem (32). We will use Hildreth's quadratic programming algorithm to solve in

real-time this problem (Luenberger 27). The main idea of this algorithm is to solve (36) for each component of $\boldsymbol{\lambda}$ iteratively, one component at a time. During iteration m, if the value of $\lambda^{(i)}$ required to minimize the cost function is negative, $\lambda^{(i)}$ is set to zero, and the algorithm proceeds to the next component $\lambda^{(i+1)}$. We employ a partitioning approach to separate the active set into two subsets: $\boldsymbol{W}_a^+$ and $\boldsymbol{W}_a^-$. These subsets correspond to the active constraints associated with $\boldsymbol{U}_{max}$ and $\boldsymbol{U}_{min}$, respectively. This results in the following partition

$$\boldsymbol{G} = \begin{bmatrix} \boldsymbol{Z} & -\boldsymbol{Z} \\ -\boldsymbol{Z} & \boldsymbol{Z} \end{bmatrix}, \quad \lambda = \begin{bmatrix} \lambda^+ \\ \lambda^- \end{bmatrix}, \quad \boldsymbol{M}\boldsymbol{E}^{-1} = \begin{bmatrix} \boldsymbol{V} \\ -\boldsymbol{V} \end{bmatrix},$$

$$\boldsymbol{\gamma} = \begin{bmatrix} \boldsymbol{\gamma}^+ \\ \boldsymbol{\gamma}^- \end{bmatrix}, \qquad \boldsymbol{\Omega} = \begin{bmatrix} \boldsymbol{\Omega}^+ \\ \boldsymbol{\Omega}^- \end{bmatrix},$$

with $\boldsymbol{Z} \in \mathbb{R}^{\ell n_u \times \ell n_u}$, $\boldsymbol{V} \in \mathbb{R}^{\ell n_u \times \ell n_u}$ and $\Omega^+ \in \mathbb{R}^{\ell n_u}$, $\Omega^- \in \mathbb{R}^{\ell n_u}$. Here, $\lambda^+ \in \mathbb{R}^{\ell n_u}$ (resp. $\lambda^- \in \mathbb{R}^{\ell n_u}$) represents the Lagrange multipliers associated with $\boldsymbol{U}_{max}$ (resp. $\boldsymbol{U}_{min}$). Problem (36) can now be reformulated as:

$$\begin{aligned} \arg\min_{\lambda \geq 0} \quad & \left(\tfrac{1}{2} \left(\lambda^{+\top} \boldsymbol{Z} \lambda^+ + \lambda^{-\top} \boldsymbol{Z} \lambda^- - 2\lambda^{+\top} \boldsymbol{Z} \lambda^- \right) \right. \\ & \left. + \lambda^{+\top} \left(\gamma^+ + \boldsymbol{V}\boldsymbol{F} \right) + \lambda^{-\top} \left(\gamma^- - \boldsymbol{V}\boldsymbol{F} \right) \right). \end{aligned} \tag{37}$$

With this formulation, Hildreth's procedure is given in Algorithm (3).

Algorithm 3 Hildreth's algorithm

Choose max_{Iter} and ϵ suitably
$m = 1$, $\boldsymbol{w}^{(1)} = \boldsymbol{\lambda}$
while $(m \leq max_{Iter})$ OR $(q > \epsilon)$ **do**
  $w_i^{+(m+1)} = -\frac{1}{z_{ii}} \left(\omega_i^+ + \sum_{j=1}^{i-1} z_{ij} w_j^{+(m+1)} + \sum_{j=i+1}^{n} z_{ij} w_j^{+(m)} - \sum_{j=1}^{n} z_{ij} w_j^{-(m)} \right)$
  $w_i^{+(m+1)} = \max\left(0, w_i^{+(m+1)}\right)$
  if $w_i^{+(m+1)} = 0$ **then**
    $w_i^{-(m+1)} = -\frac{1}{z_{ii}} \left(\omega_i^- + \sum_{j=1}^{i-1} z_{ij} w_j^{-(m+1)} + \sum_{j=i+1}^{n} z_{ij} w_j^{-(m)} \right)$
    $w_i^{-(m+1)} = \max\left(0, w_i^{-(m+1)}\right)$
  else
    $w_i^{-(m+1)} = 0$
  end if
  $\boldsymbol{w}^{(m)} = \begin{bmatrix} \boldsymbol{w}^{+(m)} \\ \boldsymbol{w}^{-(m)} \end{bmatrix}$, $q = \left\| \boldsymbol{w}^{(m+1)} - \boldsymbol{w}^{(m)} \right\|_2$, $m = m + 1$
end while
$\boldsymbol{\lambda} = \boldsymbol{w}^{(m)}$

z_{ij} is the ij^{th} element of $\boldsymbol{Z}$, ω_i^+ (resp. ω_i^-) is the i^{th} element of $\boldsymbol{\Omega}^+$ (resp. $\boldsymbol{\Omega}^-$) and $n = \ell n_u$. The optimal control sequence is then determined by Eq. (35), and the control applied to the system corresponds to the first n_u rows of the optimal sequence. This algorithm, customized for handling input saturations, facilitates the explicit formulation of the control command. To conclude this section, we summarize the control strategy in Algorithm 4.

Algorithm 4 Recursive Subspace-based Predictive Control

Phase 1 – Before closing the control loop:

Choose $\boldsymbol{Q}$, $\boldsymbol{R}$, ρ, ℓ, $\mathcal{U}$, and $\boldsymbol{Y}_r$ suitably
Calculate an offline estimation $\hat{\boldsymbol{L}}_w$ and $\hat{\boldsymbol{L}}_u$

Phase 2 – During the control loop:

for $k = \rho + \ell + 1, \cdots$ **do**
  Measure $\boldsymbol{y}(k)$
  Compute $\hat{\boldsymbol{y}}(k)$ using Algorithm 1
  Compute $\hat{\boldsymbol{e}}(k) = \boldsymbol{y}(k) - \hat{\boldsymbol{y}}(k)$ and update $\hat{\boldsymbol{E}}_{k-\ell,\ell,1}$
  Update estimates $\hat{\boldsymbol{L}}_w$ and $\hat{\boldsymbol{L}}_u$ using Algorithm 2
  Update matrices $\boldsymbol{E}$, $\boldsymbol{F}$ and vector $\boldsymbol{\gamma}$
  Compute Lagrange multipliers $\boldsymbol{\lambda}$ using Algorithm 3
  Compute $\Delta \boldsymbol{U}_{k,\ell,1}^f$ using (35)
  Apply the input $\boldsymbol{u}(k) = \Delta \boldsymbol{U}_{k,1,1}^f + \boldsymbol{u}(k-1)$ to the system
end for

5. Experimental results

In this section, we present experimental results obtained by testing the proposed control strategy in the wind tunnel under various upstream yaw angle perturbations. Initially, we outline the determination of the reference output. Subsequently, we demonstrate the control system's ability to track a given set of outputs amidst perturbations. Furthermore, we establish that when the outputs effectively track the reference, the mean base pressure $\overline{C_b}$ remains constant for all considered values of β. Additionally, we confirm that this result holds true even in the presence of dynamic perturbations. Lastly, we demonstrate the control efficacy in achieving more stringent set of objectives under the same test conditions.

The control objective is to sustain a pressure distribution at the rear of the windsor body that mirrors the distribution at zero yaw angle (β). This applies across all β values within an interval ranging from -5^o to $+5^o$. Figure 8 illustrates the time averaged pressure distribution at the base the Windsor body at $\beta = 0$. This distribution exhibits horizontal symmetry and vertical asymmetry. The output reference $\boldsymbol{Y}_r$ is established based on this pressure distribution. This configuration is expected to minimize drag variations with yaw angle.

Figure 9 displays the time averaged value of the base pressure coefficient C_b as a function of the yaw angle, both with and without control. The average is based on 180s, which corresponds to 18750 convective times. The experiments were conducted over extended periods, during which the yaw angle β remained constant. It is important to specify that the sample sizes for the past and future data are $\rho = 30$ and $\ell = 40$ samples, respectively, with a sampling rate of $10\,Hz$.
The blue curve represents the case without control, showcasing the well-known Windsor body behavior $\overline{C_b} - \beta$. The orange curve illustrates the outcomes of controlled flow, aligning with the specified objective in terms of the base pressure coefficient. Additionally, various wake states are presented. These clearly demonstrate that, without control, the wake state significantly depends on the yaw angle, displaying high asymmetry for small

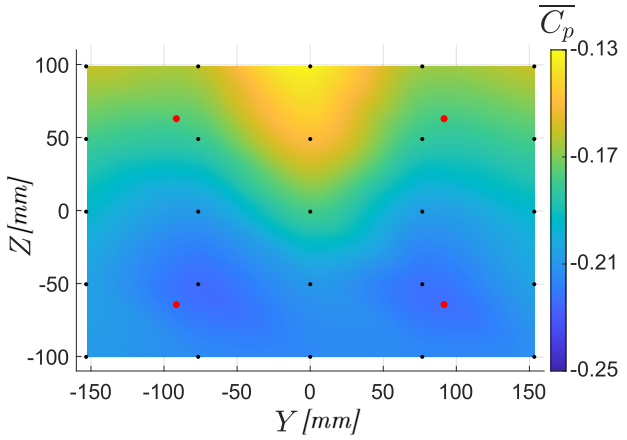

Figure 8: Pressure distribution at the rear of the Windsor body for $\beta = 0$. Red points indicate the locations of pressure sensors utilized for control.

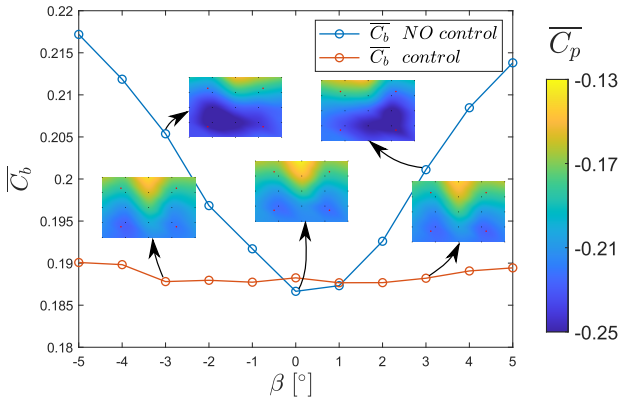

Figure 9: Mean value of the base pressure C_b versus β with (orange line) and without (blue line) control. The standard deviation of C_b is about 2% of $\overline{C_b}$ in all depicted cases.

yaw angles, such as $\beta = \pm 3°$. Conversely, in the controlled case, the mean wake state keeps its horizontal symmetry regardless of the imposed yaw angle. It's noteworthy that, in the controlled results, beyond a yaw angle of $\beta = \pm 3°$, the outcomes deviate slightly from the objective. This is attributed to the flaps lacking sufficient influence on the flow to achieve the specified objectives. Particular attention is now given to the case $\beta = -3°$. In Figure 9 we display the averaged base pressure chart and in Figure 10 we present the velocity fields measured using a PIV technique.

The pressure chart and the corresponding $\overline{C_b}$ value (Figure 9) show that the control objective are met. Moreover, the velocity field (Figure 10) indicates a noticeable symmetrization of the wake.

Moreover, we wanted to test the control law on the body underlying dynamic perturbations. With the latter, we refers to a perturbation that varies during the measurement. More precisely, in this test the yaw angle follows a sinusoidal law, defined as $y = 3sin(\frac{\pi}{100}t)$. Figure 11 depicts the response of C_b to this sinusoidal variation in β with and without control. Both curves have been obtained with a sliding average with a $3s$ window. The frequency of the perturbation is $St \simeq 10^{-3}$.

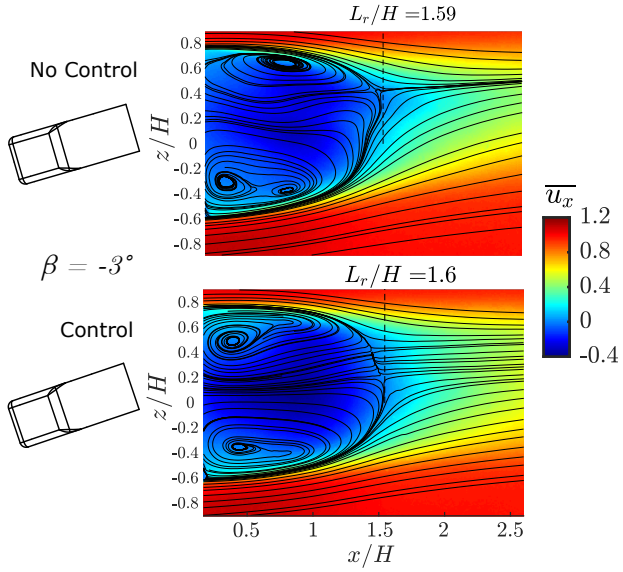

Figure 10: PIV measurements for $\beta = -3°$. Top: Uncontrolled scenario. Bottom: Controlled scenario.

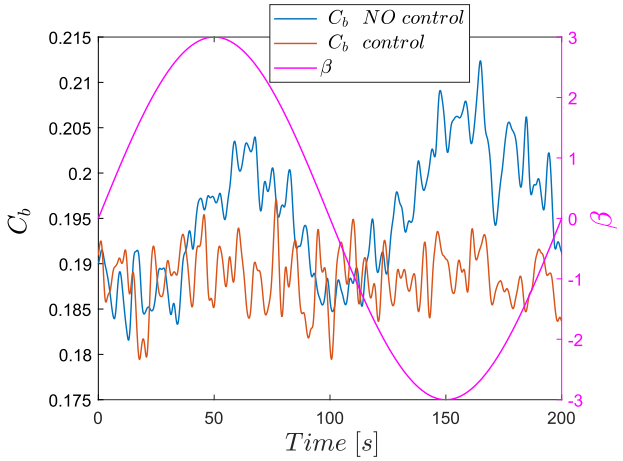

Figure 11: Mean base pressure C_b versus time in response to sinusoidal variations of β. The red line illustrates the variations of β, while the orange line represents C_b with control, and the blue line depicts C_b without control.

Notably, the control effectiveness is consistently maintained. The variability of C_b with respect to yaw angle is evident in the uncontrolled scenario, as depicted by the blue curve, while the trend stabilizes in the controlled scenario, represented by the orange curve. This observed trend results in an average improvement of approximately $\simeq 5\%$.

Another control objective, more stringent, has been tested on this model vehicle. This objective now forces both vertical and horizontal symmetry of the distribution, along with a higher pressure level. Figure 12 illustrates the outcomes pertaining to the new objective, corresponding to an output reference $\boldsymbol{Yr}_2$, in contrast to the previously discussed output reference denoted as $\boldsymbol{Yr}_1$.

The blue and orange curves mirror those presented in Figure 9, while the yellow curve reflects the results concerning the new objective. The imposition of a higher pressure level shifts

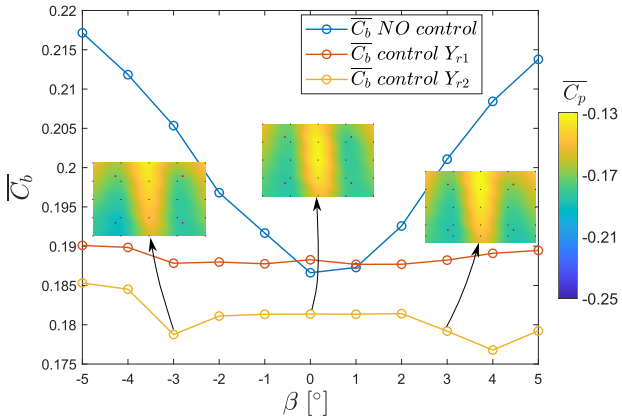

Figure 12: Mean value of the base pressure C_b versus β with and without control. $\boldsymbol{Y}_{r_1}$ corresponds to the orange line, $\boldsymbol{Y}_{r_2}$ corresponds to the yellow line and No control corresponds to the blue line. The standard deviation of C_b is about 2% of $\overline{C_b}$ in all depicted cases.

the curve downwards, indicating a significantly higher average gain. For $|\beta| \leq 2°$, the trend remains flat, whereas for $|\beta| > 2°$, some deviations from the pressure objective emerge. This indicates that in more stringent scenarios, the flaps lack authority over the wake at lower angles compared to the output reference $\boldsymbol{Y}_{r_1}$.

Also in this scenario, the new set of objectives under dynamic perturbations was tested. In what follows, the yaw angle undergoes variations every 30 seconds. Figure 13 presents the base pressure coefficient C_b obtained for step variations of β over time, with and without control. Similarly to the sinusoidal variation, both curves have been obtained with a sliding average with a $3s$ window.

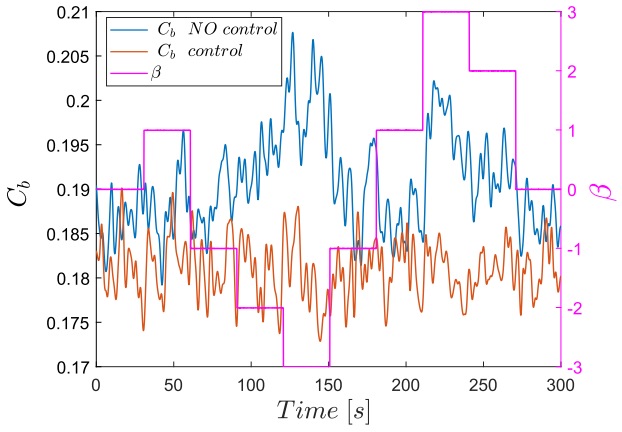

Figure 13: Mean base pressure C_b versus time in response to step variations of β. The red line illustrates step changes, while the orange line represents the scenario with control, and the blue line depicts the scenario without control.

In the non-controlled scenario, C_b exhibits significant fluctuations with β, whereas in the controlled scenario, it maintains a nearly constant value even for $\beta = \pm 3°$, consistent with the results concerning the sinusoidal yaw angle variation shown previously. The mean improvement in the controlled scenario is approximately $\simeq 7.5\%$.

In Figure 14, the control signals (depicted by the black curves) applied to the flaps are shown alongside variations in the yaw angle β, represented by the red curve. The corresponding controlled outputs are illustrated in Figure 15, while the same outputs without control are displayed in Figure 16. At the beginning of the test, the lateral flaps (u_1 and u_2) oscillate around the neutral position whereas the top/bottom ones (u_3 and u_4) address the vertical asymmetry both being oriented downwards. At $\beta = \pm 3°$ the top/bottom flaps are saturated and this explains the limitations observed in Figure 12. On the other hand, the lateral flaps don't show a symmetric behaviour. In fact both flaps' angles are positive for $\beta = -3°$ at $t \sim 130s$ while u_1 is positive and u_2 is negative for $\beta = +3°$ at $t \sim 220s$. This means that the instantaneous state of the flaps depend on the previous history. As expected, in the controlled configuration (Figure 15), the output trends remain consistent throughout the test, whereas in the uncontrolled scenario (Figure 16), the impact of the yaw angle becomes evident. This confirms what has been shown in Figure 13.

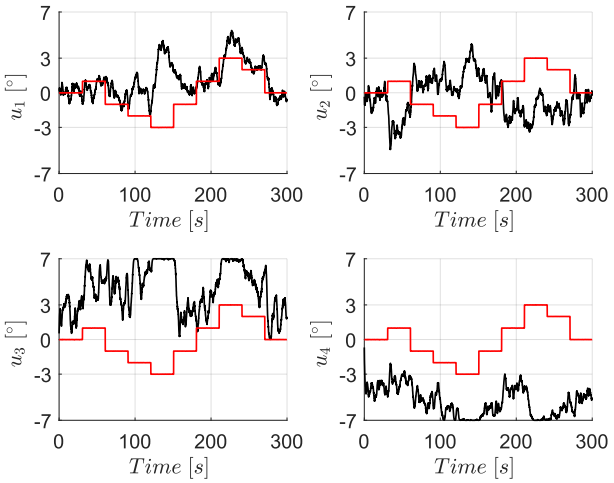

Figure 14: Command signals for flap angles (depicted by the black curves) respond to variations in β (illustrated by the red curve). We recall that u_1, u_2, u_3 and u_4 correspond to the left, right, top and bottom flaps respectively.

Although the primary focus of the paper was not on optimizing the system energetically, we will give an overview of the power dissipated by the system and we will make a comparison with the dissipated aerodynamic power under some simplifying assumptions. The power of the control system can be defined as $\mathcal{P} = \mathcal{V}I$. $\mathcal{V}$ is the voltage of the power supply (here equal to 6 V). I is the intensity of the mean current, measured as $I \simeq 0.2\ A$ during the experiments. The power dissipated by aerodynamic drag at $\beta = 0$ reads $\mathcal{P}_{a0} = V_\infty F_{x0} = V_\infty \frac{\rho}{2} V_\infty^2 S C_{D0}$. S is the frontal area of the body. The value of the drag coefficient at zero yaw is $C_{D0} = 0,26$ for this body equipped with wheels. For a variation of the base pressure coefficient δC_b, neglecting the contribution of the flaps as a first approximation, the drag force variation is $\delta F_x \approx H.W \frac{\rho}{2} V_\infty^2 \delta C_b$. Therefore, the relative aerodynamic power saving is $\delta\mathcal{P}_a/\mathcal{P}_{a0} = \delta F_x / F_{x0} \approx \delta C_b / C_{D0}$. This has to be compared with the relative control system power

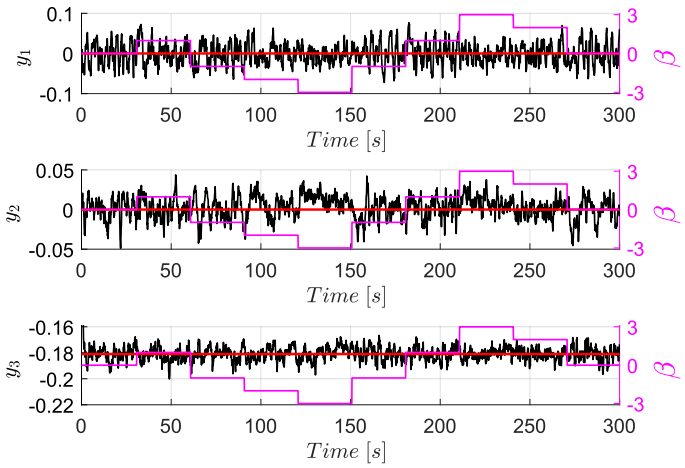

Figure 15: The controlled outputs are represented by the black curves, while the references are illustrated in red.

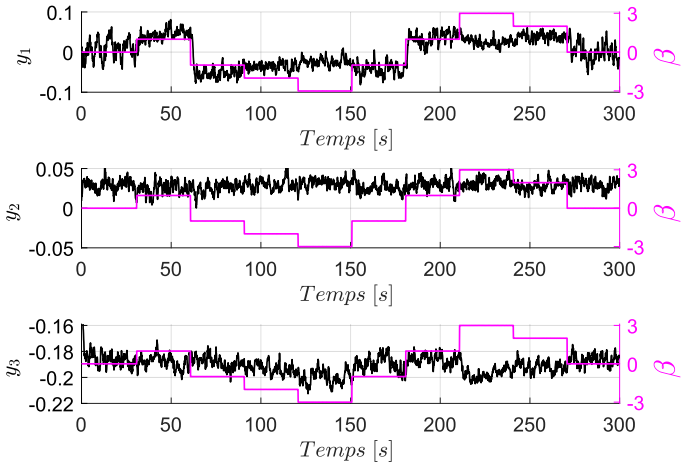

Figure 16: Output signals without control are depicted when the flap angles are set at 0°.

consumption $\mathcal{P}/\mathcal{P}_{a0}$. As a conservative estimate, for the sinusoïdal variation of β presented in figure 13, we have here $\delta\mathcal{P}_a/\mathcal{P}_{a0} \approx 4\%$ while $\mathcal{P}/\mathcal{P}_{a0} \approx 0.3\%$. Aerodynamic power savings are therefore very favourable for this model study. Of course, a specific development and optimisation should be carried out for each particular settings on scale one vehicles.

6. Conclusions

This study originated from the findings of prior road and wind tunnel experiments using both full scale vehicles and academic models, revealing an increase in drag for real driving conditions. We propose here an active solution for drag reduction consisting in controlling four rigid flaps positioned at the base of the vehicle. By employing the flaps, our goal is to manipulate the near wake orientation in order to maintain a reference pressure distribution at the base of the model. More precisely, the system output is based on four static pressure sensors only, located on the base of the model, used to represent a mean pressure level and the horizontal and vertical pressure gradients. We use an instrumented Windsor body with wheels equipped with four controlled flaps at the rear. Wind tunnel tests are conducted to generate quasi-steady disturbances.

Our results demonstrate that this system can be effectively modelled by a low-order LTV model, with parameters predominantly varying based on the upstream flow properties. We developed an adaptive control law based on SPC. To address estimation bias resulting from correlation between input/output data and noise in closed-loop, an unbiased recursive estimator was designed to dynamically adjust model parameters online. Subsequent closed-loop tests were carried out in the wind tunnel, demonstrating the viability and effectiveness of our approach. Two control objectives were presented. One consists in sustaining the basic pressure distribution at zero yaw. The other one, more stringent, forces both vertical and horizontal symmetry of the distribution, along with a higher pressure level. In both cases, the control maintains efficiently the reference pressure distribution for quasi-steady yaw angle variations representative of real driving situations. Subsequent analysis confirms a notable decrease in the base pressure coefficient C_b and, consequently, a reduction of the drag.

These promising outcomes validate the proof of concept, signifying a significant milestone. Nonetheless, substantial efforts lie ahead before implementation in production cars becomes feasible. The principal area for further improvement revolves around the actuators. Integrating active flaps in vehicles is not a practical solution. Conversely, exploring flexible tapers with the capability to locally deform the bodywork appears feasible. The efficacy of these actuators in precisely controlling the pressure at the rear of vehicles having a more complex rear geometry is yet to be substantiated. This is the subject of an ongoing research work.

Appendix A. Data equation

Regardless of the chosen state representation (12) or (A.1), controlling the system using these equations requires real-time estimation of matrices $\boldsymbol{A}$, $\boldsymbol{B}$, $\boldsymbol{C}$ and $\boldsymbol{D}$, as well as the state vector $\boldsymbol{x}(k)$. In (Favoreel et al. 14), an alternative method has been proposed to express the output $\boldsymbol{y}$ as a function of the input $\boldsymbol{u}$, thereby eliminating the need to know the state $\boldsymbol{x}$. For that, let us consider the predictor form of a LTI system given as

$$\boldsymbol{x}(k+1) = \tilde{\boldsymbol{A}}\boldsymbol{x}(k) + \tilde{\boldsymbol{B}}\boldsymbol{u}(k) + \boldsymbol{K}\boldsymbol{y}(k), \tag{A.1a}$$

$$\boldsymbol{y}(k) = \boldsymbol{C}\boldsymbol{x}(k) + \boldsymbol{D}\boldsymbol{u}(k) + \boldsymbol{e}(k), \tag{A.1b}$$

with $\tilde{\boldsymbol{A}} = \boldsymbol{A} - \boldsymbol{K}\boldsymbol{C}$ and $\tilde{\boldsymbol{B}} = \boldsymbol{B} - \boldsymbol{K}\boldsymbol{D}$ (Ljung 26). Using straightforward manipulations, the state can be expressed in terms of past input-output data over ρ samples (Chiuso 10, Jansson and Wahlberg 22)

$$\boldsymbol{x}(i+\rho) = \tilde{\boldsymbol{A}}^{\rho}\boldsymbol{x}(i) + \mathcal{K}\boldsymbol{W}_{i,\rho,1}, \tag{A.2}$$

where $\boldsymbol{W}_{i,\rho,1} = \begin{bmatrix} \boldsymbol{U}_{i,\rho,1} \\ \boldsymbol{Y}_{i,\rho,1} \end{bmatrix}$ and $\mathcal{K} = \begin{bmatrix} \mathcal{K}_\ell(\tilde{\boldsymbol{A}}, \tilde{\boldsymbol{B}}) & \mathcal{K}_\ell(\tilde{\boldsymbol{A}}, \boldsymbol{K}) \end{bmatrix}$. The Kalman gain $\boldsymbol{K}$ is designed to ensure the stability of $\tilde{\boldsymbol{A}}$. This implies the existence of a finite integer ρ such that the Frobenius norm of $\tilde{\boldsymbol{A}}^\rho$ converges to zero. Suppose we can conduct experiments on the system to collect a sequence of N input/output pairs. Consequently, employing the state approximation

$$\boldsymbol{x}(i+\rho) \approx \mathcal{K}\boldsymbol{W}_{i,\rho,1} \tag{A.3}$$

the well-known data equation can be formulated from Eq. (12), utilizing input-output data available from time instance i until $i + N - 1$ (Overchee and Moor 29).

$$\begin{aligned} \boldsymbol{Y}^f_{i,\ell,\bar{N}} &= \boldsymbol{\Gamma}_\ell(\boldsymbol{A}, \boldsymbol{C})\mathcal{K}\boldsymbol{W}^p_{i-\rho,\rho,\bar{N}} + \boldsymbol{H}_\ell(\boldsymbol{A}, \boldsymbol{B}, \boldsymbol{C}, \boldsymbol{D})\boldsymbol{U}^f_{i,\ell,\bar{N}} \\ &\quad + \boldsymbol{H}_\ell(\boldsymbol{A}, \boldsymbol{K}, \boldsymbol{C}, \boldsymbol{I})\boldsymbol{E}^f_{i,\ell,\bar{N}}, \end{aligned} \tag{A.4}$$

where $\bar{N} = N - \rho - \ell + 1$. If time step i represents the current time step, this relationship establishes a connection between past data, denoted by the index p, and future data, denoted by the index f, without involving the state.

References

[1] Åström, K.J., Wittenmark, B., 2008. Adaptive control. Courier Corporation.

[2] Bao, D., 2023. Wheel-vehicle aerodynamic interactions: consequences for drag. Ph.D. thesis. Ecole Nationale Supérieure de Mécanique et d'Aérotechnique (ENSMA).

[3] Bao, D., Borée, J., Haffner, Y., Sicot, C., 2022. Near wake interactions and drag increase regimes for a square-back bluff body. Journal of Fluid Mechanics 936 .

[4] Berkooz, G., Holmes, P., Lumley, J.L., 1993. The proper orthogonal decomposition in the analysis of turbulent flows. Annual Review of Fluid Mechanics 25, 539–575 doi:https://doi.org/10.1146/annurev.fl.25.010193.002543.

[5] Bonnavion, G., Cadot, O., Herbert, V., Parpais, S., Vigneron, R., Délery, J., 2017. Effect of a base cavity on the wake modes of the squareback Ahmed body at various ground clearances and application to drag reduction. 23ème Congrès Français de Mécanique .

[6] Carlino, G., Cardano, D., Cogotti, A., 2007. A new technique to measure the aerodynamic response of passenger cars by a continuous flow yawing. SAE Technical papers 0148-7191, 16 doi:https://doi.org/10.4271/2007-01-0902.

[7] Castelain, T., Michard, M., Szmigiel, M., Chacaton, D., Juvé, D., 2018. Identification of flow classes in the wake of a simplified truck model depending on the underbody velocity. J. Wind Eng. Ind. Aerod. 175, 352–363 .

[8] Cembalo, A., 2024. Amélioration de l'efficacité énergétique des voitures : Contrôle actif de la traînée aérodynamique en conditions amont variables. Ph.D. thesis. École Nationale Supérieure de Mécanique et d'Aérotechnique.

[9] Cembalo, A., J.Borée, Coirault, P., Dumand, C., 2023. From on-road experiments to closed loop control of base drag variations for varying upstream flow conditions, in: 5th Internacional conference in numerical and experimental aerodynamics of road vehicles and trains (Aerovehicles 5), Poitiers, France.

[10] Chiuso, A., 2007. The role of vector autoregressive modeling in predictor-based subspace identification. Automatica 43, 1034–1048 .

[11] Cooper, K., Watkins, S., 2007. The unsteady wind environment of road vehicles, part one: A review of the on-road turbulent wind environment. SAE Technical Paper 2007-01-1236, 20 doi:https://doi.org/10.4271/2007-01-1236.

[12] Garcia de la Cruz, J., Brackston, R., Morrison, J., 2017. Adaptive base-flaps under variable cross-wind. SAE Technical Papers 2017 doi:10.4271/2017-01-7000.

[13] Fan, Y., Parezanović, V., Cadot, O., 2022. Wake transitions and steady z-instability of an ahmed body in varying flow conditions. Journal of Fluid Mechanics 942, A22 doi:10.1017/jfm.2022.382.

[14] Favoreel, W., Moor, B.D., Gevers, M., 1999. Spc: Subspace predictive control. IFAC Proceedings Volumes 32, 4004–4009 doi:https://doi.org/10.1016/S1474 – 6670(17)56683 – 5.

[15] Good, G.L., Garry, K.P., 2004. On the use of reference models in automotive aerodynamics. SAE Technical Paper 2004-01-1308 .

[16] Haffner, Y., Castelain, T., Borée, J., Spohn, A., 2021. Manipulation of three-dimensional asymmetries of a turbulent wake for drag reduction. Journal of Fluid Mechanics 912, A6 doi:10.1017/jfm.2020.1133.

[17] Howell, J., Forbes, D., Passmore, M., 2017. A drag coefficient for application to the wltp driving cycle. Proceedings of the Institution of Mechanical Engineers, Part D: Journal of Automobile Engineering 231, 1274–1286 doi:10.1177/0954407017704784.

[18] Huang, B., Kadali, R., 2008. Dynamic Modeling, Predictive Control and Performance Monitoring. A Data-driven Subspace Approach. volume 374. Lecture Notes in Control and Information Sciences, Springer.

[19] Hucho, W.H., Sovran, G., 1993. Aerodynamics of road vehicles. Ann. Rev. Fluid. Mech. 25, 485–537 .

[20] Idelchik, I., Meury, M., 1969. Handbook for Hydraulic Resistance,. EYROLLES.

[21] Jansson, M., 2005. A new subspace identification method for open and closed loop data. IFAC Proceedings Volumes 38, 500–505 .

[22] Jansson, M., Wahlberg, B., 1996. A linear regression approach to state-space subspace system identification. Signal Processing 52, 103–129 .

[23] Kadijk, G., Ligterink, N., 2012. Road load determination of passenger cars. TNO Report: TNO .

[24] Khan, T.I., Parezanović, V., Pastur, L., Cadot, O., 2022. Suppression of the wake steady asymmetry of an ahmed body by central base bleed. Phys. Rev. Fluids 7, 083902 doi:10.1103/PhysRevFluids.7.083902.

[25] Li, R., Borée, J., Noack, B., Cordier, L., Harambat, F., 2019. Drag reduction mechanisms of a car model at moderate yaw by bi-frequency forcing. Phys. Rev. Fluids 4 .

[26] Ljung, L., 1999. System identification: Theory for the user, 2nd edition. Upper Saddle River: Prentice Hall .

[27] Luenberger, D.G., 1997. Optimization by vector space methods. John Wiley & Sons.

[28] Mercere, G., Markovsky, I., Ramos, J., 2016. Innovation-based subspace identification in open- and closed-loop, in: IEEE 55th Conference on Decision and Control, Las Vegas, USA.

[29] Overchee, P., Moor, B., 1996. N4sid: subspace algorithms for the identification of combined deterministic-stochastic system .

[30] Pavia, G., Passmore, M., Varney, M., Hodgson, G., 2020. Salient three-dimensional features of the turbulent wake of a simplified square-back vehicle. Journal of Fluid Mechanics 888 .

[31] Perry, A., Pavia, G., Passmore, M., 2016. Influence of short rear end tapers on the wake of a simplified square-back vehicle : wake topology and rear drag. Exp. Fluids 57 .

[32] Schröck, D., Widdecke, N., Wiedemann, J., 2007. On-road wind conditions experienced by a moving vehicle, in: FKFS-Konferenz—Progress in Vehicle Aerodynamics, Stuttgart.

[33] Stoll, D., Wiedemann, J., 2018. Active crosswind generation and its effect on the unsteady aerodynamic vehicle properties determined in an open jet wind tunnel. SAE Technical Paper doi:https://doi.org/10.4271/2018-01-0722.

[34] Urquhart, M., Sebben, S., 2022. Optimisation of trailing edge flaps on the base cavity of a vehicle for improved performance at yaw. Flow, Turbulence and Combustion 109 doi:10.1007/s10494-022-00323-z.

[35] Urquhart, M., Varney, M., Sebben, S., Passmore, M., 2021. Drag reduction mechanisms on a generic square-back vehicle using an optimised yaw-insensitive base cavity. Experiments in Fluids 62 doi:10.1007/s00348-021-03334-0.

[36] Varney, M., Passmore, M., Swakeen, R., Gaylard, A., 2020. Parametric study of reduced span side tapering on a simplified model with wheels. SAE Tech. Report. No. 2020-01-0680, Society of Automotive Engineers .

[37] Verhaegen, M., Verdult, V., 2007. Filtering and System Identification: A

Least Squares Approach. Cambridge University Press.

[38] Watkins, S., Cooper, K., 2007. The unsteady wind environment of road vehicles, part two: Effects on vehicle development and simulation of turbulence. SAE Technical Paper 2007-01-1237, 17 doi:https://doi.org/10.4271/2007-01-1237.

[39] Yamashita, T., Makihara, T., Maeda, K., Tadakuma, K., 2017. Unsteady aerodynamic response of a vehicle by natural wind generator of a full-scale wind tunnel. SAE International Journal of Passenger Cars - Mechanical Systems , 358 – 368 .

[40] Zhou, K., Doyle, J.C., 1998. Essentials of robust control. volume 104. Prentice hall Upper Saddle River, NJ.